Submitted to the 30th International Conference on High-Energy Physics ICHEP2000,
Osaka, Japan, July 2000

Search for QCD Instanton Induced Events in Deep-Inelastic Scattering at HERA

H1 Collaboration

Abstract

Signals of QCD instanton induced processes are searched for in deep-inelastic scattering (DIS) at HERA in a kinematic region defined by the Bjorken-scaling variables $x > 10^{-3}$, $0.1 < y < 0.6$ and the polar angle of the scattered positron $\theta_{el} > 156^o$. The cross section for QCD instanton induced processes in this domain is predicted to be sizeable, but two to three orders of magnitude below the standard DIS cross section. Several observables characterising hadronic final state properties of QCD instanton induced events are used to discriminate them from the standard DIS background and to identify a possibly instanton enriched domain. In a phase space region where a reduction of the standard DIS background to the percent level is achieved according to Monte Carlo models, more events are found in the data than expected by standard DIS models. The size of the excess is at a level comparable to the difference of the QCD-based standard DIS models, but is - for the discriminating observables - qualitatively similar to the expected instanton signal. For other discriminating observables the data do not particularly favour an interpretation of the excess in terms of instanton induced processes as modelled in the current implementation of the QCD instanton Monte Carlo simulation. Upper limits on the QCD instanton production cross section between $100\ \mathrm{pb}$ and $1000\ \mathrm{pb}$ are derived only from the expected instanton hadronic final state topology and the number of observed events in the data. They exclude the steep rise of the instanton cross section towards large instanton sizes as would be obtained from a naive extrapolation of instanton perturbation theory. The absense of this steep rise is in agreement with comparisons of perturbative calculations to lattice simulations.

Abstract: 972
Parallel session: 3
Plenary talk: 11

1 Introduction

The Standard Model is known to contain certain hard processes which cannot be described by perturbation theory. These violate the classical laws of baryon and lepton number conservation in case of the electroweak and chirality conservation in case of the strong interaction [1, 2, 3], respectively. Such anomalous processes are induced by instantons [4]. QCD instantons are non-perturbative fluctuations of the gluon field inducing hard processes and represent tunnelling transitions between topologically inequivalent vacua. Deep-inelastic scattering (DIS) offers a unique opportunity [5] to discover processes induced by QCD instantons through a sizeable rate, calculable[1] within "instanton-perturbation theory" [7, 8, 9], along with a characteristic final state signature [5, 10, 11]. For a recent review, see ref.[12].

At HERA, colliding 27.5 GeV positrons on 820 GeV protons, the size of the predicted cross section is large enough to make an experimental observation possible. The expected signal is, however, still small compared to the standard DIS process. The suppression of the standard DIS background is therefore the key issue in this analysis. QCD instanton-induced processes (I-processes) can be discriminated from standard DIS by their characteristic hadronic final state signature consisting of a large number of hadrons at high transverse energy emerging from a "fire-ball"-like topology [5, 10, 11, 12].

Limits on I-processes based on existing hadronic final state DIS data have already been derived in [13, 14, 15]. Here, we present for the first time a dedicated search for I-processes at HERA. The data corresponding to an integrated luminosity of 15.8 pb^{-1} were collected in the year 1997. We cover the kinematic region defined by the Bjorken-scaling variables $x > 10^{-3}$, $0.1 < y < 0.6$ and the polar angle of the scattered electron $\theta_{el} > 156^o$.

2 Production of QCD Instanton-induced Processes at HERA

Instanton induced processes in DIS are dominantly produced in a photon gluon fusion process as sketched in Fig. 1. Within the framework of A. Ringwald and F. Schrempp [5, 7, 8, 9, 11, 12] the instanton induced event signature may be described by the following basic reaction:

$$\gamma^* + g \to \sum_{n_{\text{flavours}}} (\bar{q}_R + q_R) + \; n_g \, g, \tag{1}$$

where q_R ($\bar{q}_R$) denotes right handed quarks [2] and g gluons. A photon splitting into a quark-anti-quark pair in the background of an instanton or an anti-instanton fuses with a gluon from the proton. Besides the current-quark (q''), the partonic final state consists of $2n_f - 1$ right-handed (massless) quarks and anti-quarks. In every I-induced event, one quark anti-quark pair of all $n_f (= 3)$ flavours is simultaneously produced [3]. In addition, a mean of $\langle n_g \rangle^{(I)} \sim \mathcal{O}(1/\alpha_s) \sim 3$ gluons are emitted in the I-process. These partons emerge isotropically distributed from the

[1] For an exploratory calculation of the instanton contribution to the gluon structure function at large $x_g > 0.3 - 0.35$, see ref. [6].

[2] Right handed quarks are produced in instanton processes. Left-handed quarks are produced in anti-instanton processes. The hadronic final state referring to instantons and anti-instantons respectively, can only be distinguished by the chirality of the quarks. Both processes enter in the cross section.

[3] If kinematically possible, charm and bottom quarks can also be produced. The estimation of the cross section is, however, difficult and is not considered here.

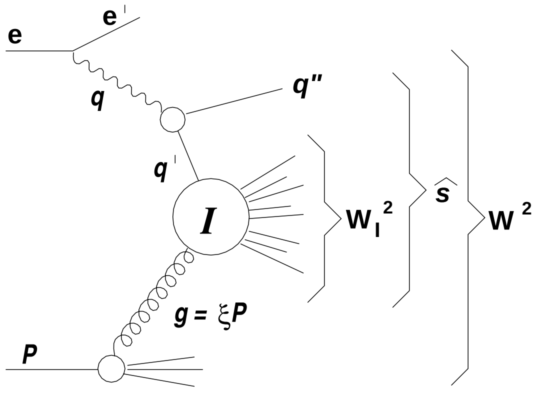

DIS variables:
$S = (e + P)^2$
$Q^2 = -q^2 = -(e - e')^2$
$x = Q^2 / \, (2P \cdot q)$
$W^2 = (q + P)^2 = Q^2(1 - x)/x$
$\hat{s} = (q + g)^2$
$\xi = x \; (1 + \hat{s}/Q^2)$

Variables of I-subprocess:
$Q'^2 \; = -q'^2 = -(q - q'')^2$
$x' = Q'^2 \; / \; (2 \; g \cdot q')$
$W_I^2 = (q' + g)^2 = Q'^2 \; (1 - x' \;)/x'$

Figure 1: Kinematic variables of the dominant instanton induced process in deep-inelastic scattering. The virtual photon γ (4-momentum $q = e - e'$), emitted by the incoming electron e, fuses with a gluon (4-momentum g) of the proton (4-momentum P). The gluon carries a fraction ξ of the (longitudinal) proton 4-momentum. The virtual quark entering the instanton subprocess has 4-momentum q', while the outgoing quark (= *current quark*) from the $\gamma \to q\overline{q}$-process has q''. x' is defined in analogy with x, but cannot be illustrated in a simple way. $0 \leq x \leq x/\xi \leq x' \leq 1$ holds. W_I is the invariant mass of the quark gluon ($q'g$) system and W is the invariant mass of the total hadronic system (the γP system). $\hat{s}$ is the invariant mass squared of the γg system.

I-process. One expects therefore a pseudo-rapidity [4] (η) region (with a width of $\approx 1.1 \; \eta$ units) densely populated with particles at high transverse momentum which are homogeneously distributed in azimuth. Besides this pseudo-rapidity band, the hadronic final state of I-induced events exhibits a current jet emerging from the outgoing current quark. The high density of partons emitted in the I-process leads to a high mean multiplicity of charged particles in every event. Moreover, since all (effectively massless) flavours are produced in any event, more mesons containing strange quarks should be found in I-induced events than in normal DIS events.

The actual number of produced hadrons and their energy crucially depends on the squared centre of mass energy $W_I^2 \; = \; (q' + \xi p)^2$ available in the I-system. $W_I^2 \; = \; Q'^2 \; (1 \; - \; x' \;)/x'$ is closely connected to the variables Q'^2 and x' describing the kinematics of the I-subprocess. These variables are analogous to the Bjorken scaling variables x and Q^2. The knowledge of the distribution of these variables is therefore indispensable for the correct prediction of the hadronic final state. Since the I-cross section can been calculated for large Q'^2 and x' this distribution is known within I-perturbation theory [8]. Towards low values, however, the I-cross section is steeply increasing. In this region the approximations made to derive the cross section in I-perturbation theory no longer valid. The fiducial region where I-perturbation theory is expected to work has been estimated from a high quality lattice simulation of crucial quantities entering in the instanton calculations [9].

For the fiducial region, $x' \; > \; 0.35$, $Q'^2 \; > \; 113 \;\; \mathrm{GeV}^2$, $x \; > \; 10^{-3}$ and $0.1 \; < \; y \; < \; 0.9$, an update of the published I-cross section [8], referring to the 1998 world average of the strong

[4] The pseudo-rapidity of a particle is defined as $\eta \; \equiv \; -\ln(\tan\theta/2)$ where θ is the polar angle with respect to the proton direction.

coupling constant [16], has been given in [12, 17] to be: $\sigma_{ins} = 89^{+18}_{-15}$ pb. To further reduce remaining theoretical uncertainties, ideally, an additional cut, $Q^2 > 113\ \mathrm{GeV}^2$, has to be applied. In this domain the cross section is: $\sigma_{ins} = 29^{+10}_{-7.5}$ pb. The quoted error only contains the uncertainties of σ_{ins} obtained from varying the strong coupling constant within the error of the world average. This cross section has been derived for three-flavours. The calculation is based on a two loop renormalisation group invariant expression of the instanton density.

While this prediction has not yet reached the same quantitative level as current standard perturbative QCD calculations, the cross section is large enough to make dedicated searches for instanton induced processes interesting.

3 QCD Monte Carlo Models

3.1 Standard DIS Monte Carlo Models

A simulation of the detailed properties of the hadronic final state in DIS is available in the form of QCD Monte Carlo event generators. These include the matrix element of the hard subprocess to first order in the strong coupling constant α_s, approximations of higher order QCD radiation effects, and a model to describe the non-perturbative transition from partons to hadrons.

The RAPGAP Monte Carlo [18] incorporates the $\mathcal{O}(\alpha_s)$ QCD matrix element and models higher order parton emissions approximately to all orders α_s using the concept of parton showers [19] based on the leading logarithm DGLAP equations [20]. QCD radiation can occur before and after the hard subprocess. The formation of hadrons is performed using the LUND string model [21] implemented in JETSET [22]. This QCD Monte Carlo is called “MEPS” in the following.

A completely different treatment of the perturbative phase is implemented in ARIADNE [23], where gluon emissions are simulated using the colour dipole model (CDM) [24] assuming a chain of independently radiating dipoles spanned by colour connected partons. No distinction between initial and final state partons is made. The first emission in the cascade is corrected to reproduce the matrix element to first order α_s [25]. The hadronisation is performed using JETSET. This QCD Monte Carlo is called “CDM” in the following.

The program HERACLES [26] is interfaced to ARIADNE and RAPGAP to include $\mathcal{O}(\alpha)$ electroweak corrections to the lepton vertex.

The PHOJET [27] Monte Carlo program is used to calculate the photoproduction background. It contains the first order matrix elements for direct and resolved processes, parton showers and a phenomenological description of soft processes.

Both Monte Carlo DIS samples have been generated with the CTEQ4M [28] parton density function and are reweighted using a parametrisation of the $96/97$ proton structure function as measured in a recent H1 analysis.

All above the standard DIS Monte Carlo generators are based on leading order calculations. The correct QCD dynamics, in particular in the small-x regime, is still under debate at

HERA. The MEPS and the CDM models have been comprehensively compared to a variety of hadronic final state data and an attempt has been made to optimise free model parameters [29]. No parameter set was found that describes the whole range of distributions over the full studied kinematic domain $5 \lesssim Q^2 \lesssim 5000\ \mathrm{GeV}^2$. It is therefore questionable to what extent the currently available QCD models can give a fair representation of the standard DIS hadronic final state. In this analysis the Monte Carlo models have been used with their default values.

3.2 QCD Instanton Monte Carlo Model

QCDINS [30, 31] is a Monte Carlo package for simulating QCD-instanton induced scattering processes in DIS. It acts as a hard process generator embedded in the HERWIG [32] program. The hard process is treated according to the physics assumptions explained in section 2. We use the default values of the QCDINS 2.0 version, i.e. $x' > 0.35$, $Q'^2 > 113\ \mathrm{GeV}^2$ and $n_f = 3$. The CTEQ4L [28] parton density function is used. After assembling the hard I-subprocess, further gluon emissions are simulated in the leading-logarithm approximation. The coherent branching algorithm implemented in HERWIG is used. The transition from partons to the observable hadrons is performed with the cluster fragmentation model [33], where the primary hadrons are produced from mainly isotropic two-body decays of colour-singlet parton clusters. As an alternative the LUND string model can be also be used. QED radiation is not implemented.

It is not clear whether the currently used hadronisation models implemented in HEP event simulation programs are appropriate to describe the fragmentation of the large number of $\mathcal{O}(10)$ partons produced by the I-process in a narrow pseudo-rapidity region with high transverse energy. However, the observables studied are mainly influenced by the hard instanton-subprocess and depend only slightly on the hadronisation model [11]. This has been studied by using JETSET instead of the cluster fragmentation model and by changing free parameters in the hadronisation models.

4 The H1 Detector

A detailed description of the H1 detector can be found elsewhere [34]. Here we briefly introduce the detector components most relevant for this analysis: The liquid argon (LAr) calorimeter, the backward lead-fibre calorimeter (SpaCal) and the tracking chamber system.

The LAr calorimeter [35] consists of an electromagnetic section ($20-30$ radiation lengths) with lead absorber and a hadronic section with steel absorber. The total depth of both calorimeters varies between 4.5 and 8 interaction lengths. The hadronic energy flow is mainly measured by the LAr calorimeter extending over the polar angle range $4^\circ < \theta < 154^\circ$ with full azimuthal coverage. Electromagnetic shower energies are measured with a resolution of $\sigma_E/E \approx 0.12/\sqrt{E\,[\text{ GeV }]} \oplus 1\%$ [36]. Test beam measurements of the LAr calorimeter modules show an energy resolution of $\sigma_E/E \approx 0.50/\sqrt{E\,[\text{ GeV }]} \oplus 0.02$ after software weighting for charged pions [37].

The backward lead-fibre calorimeter SpaCal [38] covers the polar angle range $153^\circ < \theta < 177^\circ$. In the electromagnetic section, with a depth of 28 radiation lengths, electrons are measured with an energy resolution of $\sigma_E/E \approx 0.075/\sqrt{E\,[\text{ GeV }]} \oplus 2.5\%$. In addition the SpaCal has a hadronic section of two interaction lengths to measure hadrons.

The calorimeters are surrounded by a superconducting solenoid providing a uniform magnetic field of 1.15 T parallel to the beam axis in the tracking region.

Charged particle tracks are measured in two concentric jet drift chamber modules (CJC), covering the polar angle range $15^\circ < \theta < 165^\circ$ [39]. A backward drift chamber BDC aids identification of positrons scattered into the SpaCal calorimeter.

The luminosity is measured using the elastic Bethe-Heitler process. The final state positron and photon are detected in calorimeters situated close to the beam pipe at distances of 33 m and 103 m from the interaction point in the positron beam direction.

5 DIS Event Selection

The data used in this analysis were collected in the year 1997 with the H1 detector at the ep collider HERA. During this time HERA collided positrons at an energy of $E_e = 27.5$ GeV with protons at an energy of $E_p = 820$ GeV. The accumulated data sample corresponds to an integrated luminosity of about 15.8 pb^{-1}.

The scattered positron is identified as the electromagnetic energy deposition with the highest energy in the SpaCal calorimeter. It is required to lie well within the calorimeter and trigger acceptance of polar angles between 156° and 176°. A minimal positron energy of $E'_e \geq 10$ GeV is required. To suppress background from misidentified photoproduction events the distance to the closest signal in the preceding drift chamber (BDC) has to be smaller than 3 cm. The events are triggered by demanding a localised energy deposition in the SpaCal together with loose track requirements in the multi-wire proportional and the drift chambers.

Furthermore 35 GeV $< \sum(E - p_z) <$ 70 GeV, where the sum runs over all objects belonging to the hadronic final state (see section 6), is required. The position of the z coordinate of the reconstructed event vertex must be within ± 30 cm of the nominal interaction point.

The photon virtuality Q^2 and the Bjorken scaling variable x are reconstructed from the scattered positron. The analysis is performed in the phase space region defined by $\theta_{el} > 156^o$, $0.1 < y < 0.6$ and $x > 10^{-3}$, where θ_{el} is the polar angle of the scattered positron.

The DIS data sample consists of 275000 events. The simulated events reproduce the distributions in energy and angle of the scattered positron as well as the kinematic variables x, Q^2 and y to the 3% level. The contamination by events with misidentified positrons stemming from γp reactions is below 2% and is neglected in the following. This was estimated using the Monte Carlo simulation program PHOJET [27].

6 Definition of the Discriminating Observables

The observables used to discriminate I-induced events from standard deep-inelastic scattering are based on the hadronic final state. For most of the observables the energy flow in the detector is reconstructed by combining the calorimetric energy depositions in the LAr and the SpaCal calorimeters and the momenta of low momentum tracks ($p_t < 2$ GeV) in the central jet chamber according to the procedure described in [40]. Charged particles with transverse momenta of $p_t > 0.15$ GeV are identified within the acceptance of the central jet chamber ($20^o < \theta < 155^o$). The hadronic final state objects are boosted to the hadronic centre-of-mass (hcms) frame[5].

Jets are defined by the cone algorithm [41, 42] with a cone radius of $R = \sqrt{\eta^2 + \phi^2} = 0.5$. The jet with the highest transverse energy (Et_{jet}) is used to estimate the 4-momentum q'' of the current quark (see Fig. 1). Once the current jet is found, Q'^2 can be reconstructed from the particles associated to the current jet and the photon reconstructed using the momentum of the scattered positrons. We treat Q'^2_{rec} as a good discriminating observable. Due to the limited accuracy of the Q'^2 reconstruction, Q'^2_{rec} can not be used to experimentally control the "true" Q'^2 region of the I-processes. The achieved Q'^2 resolution is about $20 - 30\%$. However, the distribution of the true over the reconstructed value exhibits large tails. The relatively small cone radius of $R = 0.5$ gives the best result. More information on the Q'^2 reconstruction can be found in [11, 43]. The reconstruction of the variable x' is very difficult[6].

The objects belonging to the jet are not used in the following observables. The E_t-weighted rapidity mean $\bar{\eta} = \sum_h E_{t,h} \ \eta_h / \sum E_{t,h}$ of all remaining objects is used as an estimator of the position of the instanton band, which is defined by $\bar{\eta} \pm 1.1$. Within this rapidity region the number of charged particles (n_b) is counted and the total scalar transverse energy (Et_b) is

[5] The hcms is defined by $\vec{q} + \vec{p} = 0$, where $\vec{q}\ (\vec{p})$ is the 4-momentum of the photon (proton).

[6] Due to the inherent difficulties to reconstruct x' experimentally, the data used for the present analysis do not incorporate a cut on x', necessary to warrant the validity of I-perturbation theory. As noticed in Ref. [9], this presumably does not prevent a comparison with the Ringwald-Schrempp predictions for the following reason. The lattice data for the $I\bar{I}$-distance distribution (from which the minimal theoretical x'-cut was deduced [9]) happen to exhibit an extremely rapid suppression of I-effects for small $I\bar{I}$-separation, corresponding to $x' < 0.35$. Therefore, I-contributions to the data from this x' region outside the validity of I-perturbation theory are probably also small.

measured. Furthermore, the axis $\vec{i}$ is found for which the summed projections of the 4-momenta of all hadronic objects are minimal resp. maximal [10]. The relative difference between $E_{in} = \min_i \sum_h |\vec{p}_h \cdot \vec{i}|$ and $E_{out} = \max_i \sum_h |\vec{p}_h \cdot \vec{i}|$ is called $\Delta_b = (E_{in} - E_{out})/E_{in}$. This quantity measures the E_t weighted azimuthal isotropy of an event. For isotropic events Δ_b is expected to take small values while for pencil-like events Δ_b should be large.

The vectorial sum of all measured final state objects not associated to the "current" jet (see above) is used to perform a boost to their rest system defined by $\sum_h \vec{p}_h = 0$. In this system, which is an approximation to the instanton rest system defined by: $\vec{q'} + \vec{g} = 0$ (see Fig.1), the sphericity Sph is calculated.

7 Search Strategy and Results

7.1 Description of the Observables in the Inclusive DIS Sample

The search strategy is based on three of the six observables presented in section 6: the multiplicity in the band (n_b), the sphericity as calculated in the rest system of all final state objects not associated to the current jet (Sph) and the reconstructed Q'^2_{rec}. These observables will be exploited to define an possibly instanton enriched data sample.

The distributions of the discriminating observables for data, for the standard DIS Monte Carlo simulation and for the I-process are shown in Fig. 2 and Fig. 3. They are all fairly well described by the standard DIS Monte Carlo simulations. Both standard DIS models overshoot the data for $1 < n_b < 5$ and undershoot the data for $5 < n_b < 10$ by $5 - 10\%$. For the highest charged particle multiplicities discrepancies up to 20% are found. For sphericity values between $0.1 <$ Sph < 0.4 the standard DIS Monte Carlo models predict $5 - 10\%$ more events than found in the data, while for Sph > 0.4 $5 - 20\%$ less events than in the data are predicted. For values below $100\ \text{GeV}^2$ the Q'^2_{rec} distribution is described within 5%, for higher values differences of up to 10% are found.

The three other observables not used to define the instanton-enriched data sample, i.e. Et_{jet}, Et_b and Δ_b, contain additional information. They are shown in Fig. 4 and Fig. 5. The Δ_b distribution is fairly well described (within 10%) by both standard DIS simulations. For the Et_{jet} the two standard DIS Monte Carlos simulations behave differently. MEPS is about 10% below (above) the data for $Et_{jet} < 2.5$ GeV ($Et_{jet} > 2.5$ GeV). In the tail of this distribution the data are well reproduced up to the largest accessible values. CDM describes the data within 5% for $Et_{jet} \lesssim 7.5$ GeV, but then exhibits an increasingly too hard Et_{jet} spectrum toward larger Et_{jet}. However, for Et_{jet} ranges where an I-signal is expected, the difference between the data and the CDM simulation is not bigger than 20%. A harder tail than found in the data is also seen in the Et_b distribution. Again the MEPS simulation gives a good description in this domain ($Et_b > 10$ GeV). The hard transverse energy tail produced by CDM has also been observed in dijet production [44]. It can be brought in agreement with the data by adjusting free model parameters [29]. For $2 < Et_b < 10$ GeV deviations between the data and the standard DIS models within 10% are seen. The data are, however, always in between the standard DIS simulations. At very low Et_b values ($Et_b < 2$ GeV) the data exceed the simulations by 20%.

	CUT A	CUT B	CUT C
n_b	$n_b \geq 5$	$n_b \geq 7$	$n_b \geq 8$
Q'^2_{rec}	$95 < Q'^2_{rec} < 200$ GeV^2	$105 < Q'^2_{rec} < 200$ GeV^2	$105 < Q'^2_{rec} < 200$ GeV^2
Sph	Sph > 0.4	Sph > 0.4	Sph > 0.5
ϵ_{ins}	31.5%	20.5%	11.2%
ϵ_{dis}	0.8-0.9 %	0.36-0.4 %	0.13-0.16%

Table 1: Cut values, instanton (standard DIS) ϵ_{ins} (ϵ_{dis}) efficiency in the three cut scenarios.

The instanton prediction is shown as a solid line in Fig.4. One can see that the expected instanton signal is about two to three orders of magnitude smaller than the standard DIS background. Therefore additional cuts are needed to enhance the signal over the background.

7.2 Search Strategy Based on Simple Cuts

The strategy to reduce the standard DIS background is based on the three observables shown in Fig. 6. The shape of these observable is different for I-processes and standard DIS. To find the optimal cut scenario 125 combinations of 5 different values of the three observables are investigated using simulations of the standard DIS background and of the I-signal. The following cuts are applied: $n_b > 5, 6, 7, 8, 9$; Sph $> 0.4, 0.5, 0.55, 0.6, 0.65$; $95, 100, 105, 110, 115 < Q'^2_{rec} < 200 \text{ GeV}^2$. From 125 cut combinations three scenarios are chosen according to the following criteria:
(A) The highest instanton efficiency (ϵ_{ins})
(B) High ϵ_{ins} at reasonable background reduction (ϵ_{dis})
(C) Highest separation power ($\epsilon_{ins}/\epsilon_{dis}$) at $\epsilon_{ins} \approx 10\%$.

The cut values, the instanton efficiency ϵ_{ins} and the standard DIS efficiency ϵ_{dis} for each chosen cut combination are summarised in table 1. A background reduction to the permille level is achieved while a sizeable instanton efficiency is ensured. A maximal separation power $\epsilon_{ins}/\epsilon_{dis}$ of 86 is reached.

7.3 Experimental Results

The numbers of events in the data and in the standard DIS Monte Carlo simulation for the three cut scenarios are summarised in table 2. The quoted errors on the expected event numbers include the statistical and the systematical uncertainties. The experimental sources of the uncertainties are: 4% on the absolute value of the hadronic energy scale measured in the LAr calorimeter, 1% on the electromagnetic energy scale, 7% on the hadronic energy measured in the SpaCal calorimeter, 3% for the measurement of the track momentum and 2 mrad for the polar angle of the scattered positron. Moreover, an absolute normalisation error of 1.5% for the accuracy of the luminosity determination has been included. In the Monte Carlo the parton density function have been reweighted to the ones measured by H1. An overall error of 3% is assigned for the limited precision of the proton structure function measurement. The systematic error is dominated by the uncertainty in the electromagnetic energy scale.

(A) DATA: 3000		(B) DATA: 1332		(C) DATA: 549	
CDM	MEPS	CDM	MEPS	CDM	MEPS
2469^{+242}_{-238}	2572^{+237}_{-222}	1005^{+82}_{-70}	1084^{+75}_{-46}	363^{+22}_{-26}	435^{+36}_{-22}

Table 2: Measured number of data events and expected standard DIS background for three cut scenarios. The errors are dominated by systematic uncertainties.

After the cuts of scenario A, 3000 events are left in the data while 2469^{+242}_{-238} (2572^{+237}_{-222}) are expected by the CDM (MEPS) Monte Carlo simulation. The distribution of the three cut observables is shown in Fig. 7. The excess in the data is mainly concentrated at low n_b, at low Q'^2_{rec} values and is approximately equally large over the entire sphericity range.

After the cuts of scenario B, 1332 events are left in the data while 1005^{+82}_{-70} (1084^{+75}_{-46}) are expected by the CDM (MEPS) Monte Carlo. The distribution of the three cut observables is shown in Fig. 8. The excess of the data over the standard DIS Monte Carlo is most pronounced at low n_b and at low Q'^2_{rec} values.

After the cuts of scenario C, 549 events are left in the data while 363^{+22}_{-26} (435^{+36}_{-22}) are expected by the CDM (MEPS) Monte Carlo. The distribution of the three cut observables is shown in Fig. 9. The difference between data and standard DIS expectation is most pronounced at the lowest bin in n_b and for $0.5 <$ Sph < 0.6 and $100 < Q'^2_{rec} < 150$ GeV^2.

In all three cut scenarios more events are observed than expected by the standard DIS Monte Carlo models. The relatively large systematic experimental uncertainties ($5 - 10\%$) reduce the significance of the excess. However, they are not able to explain the difference between data and standard DIS Monte Carlo simulation. The two available standard DIS Monte Carlo models based on leading order QCD matrix elements and implementing different treatments of the higher order parton emissions agree with each other within 20%. They are both not able to explain the data. With increasing separation of instanton induced processes over normal DIS events an increasingly large excess is seen in the data. A qualitative similarity between the difference between data and DIS Monte Carlo simulation and the expected shape of the I-signal is observed. From a purely statistical point of view the excess is significant, however the uncertainties in the background estimation are largely unknown in this extreme phase space region. Whether this excess can be explained by instanton induced processes or is simply due to an incomplete implementation of higher order parton emissions or due to, for example, an incorrect treatment of heavy quarks in the QCD Monte Carlo models remains an open question.

The other three observables which are sensitive discriminators for instantons from DIS events are shown in Figs. 10, 11,12. The biggest discrepancy between data and standard DIS Monte Carlo simulation is found at the lowest transverse energy in the instanton band where the expected contribution from I-processes is small. For $Et_b > 10$ GeV, where the instanton signal is expected to be largest, CDM predicts more events and MEPS less events than found in the data. Only in the cut scenario with the highest sensitivity the data slightly exceed both standard DIS expectations in this domain. The difference between the two standard DIS Monte Carlo simulations is not much smaller than the expected instanton signal. The shape of the Et_b observable does therefore not particularly support the hypothesis that the observed excess can be explained by I-processes as currently implemented in the QCDINS Monte Carlo simulation. The theoretical uncertainties on the default x' , Q'^2 parameters of QCDINS can, however, change the hadronic final state as discussed in [17].

7.4 Extraction of the Upper Limit

The hadronic final state of instanton induced events is strongly influenced by the energy $W_I^2 = Q'^2\ (1 - x'\ )/x'$ available for the partons emerging from the instanton subprocess. The final state topology does therefore crucially depend on both the minimal cut values, where instanton perturbation theory is expected to be valid, and on the assumed x' and Q'^2 distributions which are only under theoretical control for large x' and Q'^2.

To minimize the theoretical input in the extraction of an upper limit on the instanton production cross section, small ranges of approximately constant Q'^2 and x' are analysed. Events in a $5\ \times\ 5$ grid with $0.2 \leq x'\ \leq 0.45$ (grid size 0.05) and with $60 \leq Q'^2\ \leq 160\ \ \mathrm{GeV}^2$ (grid size $20\ \ \mathrm{GeV}^2$) have been simulated using QCDINS.

For each bin separately, events from one particular instanton type defined by the chosen x' and Q'^2 values are compared to all simulated standard DIS events. The same strategy as described in section 7.2 is applied to find the optimal cuts to enhance the I-signal over the background using the observables n_b, Q'^2_{rec} and Sph. The combination ensuring an instanton efficiency $\epsilon_{ins} > 10\%$ and the maximal separation power $\epsilon_{ins}/\epsilon_{dis}$ is chosen. For each of the 25 different resulting cuts the number of observed events in the data and of the expected number of standard DIS events is determined and an upper limit on the instanton production cross section at 95% confidence level (CL) is derived. Two upper limits based on the two available standard DIS QCD simulations are extracted and the difference between the two is treated as systematic uncertainty. The result is shown in Fig. 13 as a function of x' in bins of Q'^2 as hatched area. Regions above the hatched area are excluded.

Given the known deficiencies of the standard DIS models to describe the hadronic final state in the HERA DIS regime, it is, however, questionable whether the CDM and MEPS models are able to adequately describe the standard DIS background in this extreme corner of phase space where (depending on the x',Q'^2 bin) only $0.7 - 0.04\%$ of the events in the total sample of DIS events are expected to remain. These models were - before any cuts - only able to describe the observables used in this analysis to an accuracy of 20%. Moreover, after the cuts applied to enhance the expected instanton signal large differences at low values of the transverse energy in the band were found between the two models. To be independent of the concrete modelling of the hadronic final state of DIS events, an additional upper limit is extracted where the expected standard DIS background is set to zero. Whatever the “true” number of standard DIS events in the selected corner of phase space is, the instanton signal can certainly not be much bigger than the number of observed events in the data. This upper limit on the instanton production cross section is therefore the most conservative one, since it only uses the expected topology of instanton events and the number of events observed in the data. The limit is shown as a solid line in Fig. 13. Regions above the curve are excluded.

Instanton cross sections between 100 and $1000\ \ \mathrm{pb}$ can be excluded. In Fig. 13 also the instanton cross section evaluated in the Ringwald-Schrempp framework is indicated in the region where I-perturbation theory is expected to be valid, i.e. for large x' and Q'^2. The upper limits are above the predicted cross sections in the fiducial region $x' > 0.35$ and $Q'^2 > 113$ GeV^2. However, these results can exclude the continuation of the fast increase of the instanton cross section towards lower values of x' and Q'^2 as expected from a naive extrapolation of I-perturbation theory into this domain. This is the first experimental hint that the steep rise of the I-cross section has to be attenuated in this domain. This agrees with QCD calculations performed for zero flavours on the lattice [9].

8 Conclusions

We have searched for QCD instanton induced processes as modelled in the Monte Carlo simulation program QCDINS in deep-inelastic scattering in the kinematic range $x > 10^{-3}$, $0.1 < y < 0.6$ and $\theta_{el} > 156^o$. We used three observables, the multiplicity in the instanton band n_b, the reconstructed quark virtuality entering the instanton subprocess Q'^2_{rec} and the sphericity in the approximately reconstructed instanton rest system Sph, to select a QCD instanton enriched data sample. Using a simple cut technique the standard DIS background can be suppressed to the 0.1% level, while 10% of the instanton induced events are expected to be selected. In this region 549 events are observed and 363^{+22}_{-26} and 435^{+36}_{-22} are expected from the standard DIS background models the colour dipol model and the matrix element and parton shower model, respectively. With increasing sensitivity of instanton induced processes over standard DIS events an increasingly large excess is seen in the data. The shape of the excess in the observables n_b, Sph and Q'^2_{rec} is qualitatively compatible with the expected instanton signal. However, the size of this signal is at the level of discrepancies between the QCD models. The shapes of other observables (not used in the cuts) are neither well reproduced by CDM nor by MEPS. Also the observed excess in the transverse energy in the instanton band is not particularly favoured by the QCDINS predictions. However, the QCDINS predictions can not be excluded given the uncertainties in the cross section calculation and the modelling of the hadronic final state.

For various assumptions on the variables x' and Q'^2 characterising the hard instanton processes an upper limit on the instanton cross section is derived which makes only use of the expected instanton hadronic final state topology and the number of observed events in the data. Instanton cross sections between 100 and 1000 pb can be excluded. This limit is larger than the predicted instanton cross section, but excludes a steep rise as would be obtained from a naive extrapolation of I-perturbation theory. The absence of such steep rise is in accord with lattice simulations for zero flavours.

It should also be noted that the QCD Monte Carlo models have known deficiencies and fail to describe many aspects of DIS data in the HERA regime. A better understanding of the formation of the hadronic final state in DIS at the extreme end of the phase space relevant for instanton searches is required. The expected background in the instanton enriched sample is still large and in future more observables and better discrimination techniques should be used to further reduce the standard DIS background.

9 Acknowledgements

We thank A. Ringwald and F. Schrempp for many inspiring discussions and for their help.

We are grateful to the HERA machine group whose outstanding efforts have made and continue to make this experiment possible. We thank the engineers and technicians for their work in constructing and now maintaining the H1 detector, our funding agencies for financial support, the DESY technical stuff for continual assistance, and the DESY directorate for the hospitality which they extend to the non-DESY members of the collaboration.

References

[1] G. 'T HOOFT, *Phys. Rev. Lett. 37* (1976) 8.

[2] G. 'T HOOFT, *Phys. Rev.* ***D** 14* (1976) 3432.

[3] G. 'T HOOFT, *Phys. Rev.* ***D** 18* (1978) 2199 (Erratum).

[4] A. BELAVIN, A. POLYAKOV, A. SCHWARZ AND YU. TYUPKIN, *Phys. Lett.* ***B** 59* (1975) 85.

[5] A. RINGWALD AND F. SCHREMPP, In *Quarks '94* (Vladimir, Russia, 1994), D. Grigoriev et al., Eds., Proc. of the 8th Int. Seminar, pp. 170–193, hep–ph/9411217.

[6] I. BALITSKY AND V. BRAUN, *Phys. Lett.* ***B** 314* (1993) 237.

[7] S. MOCH, A. RINGWALD AND F. SCHREMPP, *Nucl. Phys.* ***B** 507* (1997) 134.

[8] A. RINGWALD AND F. SCHREMPP, *Phys. Lett.* ***B** 438* (1998) 217.

[9] A. RINGWALD AND F. SCHREMPP, *Phys. Lett.* ***B** 459* (1999) 249.

[10] M. GIBBS ET AL., In *Future Physics at HERA* (Hamburg, 1996), G. Ingelman, A. D. Roeck, and R. Klanner, Eds., vol. 1, p. 509.

[11] T. CARLI, J. GERIGK, A. RINGWALD AND F. SCHREMPP, *In: Monte Carlo Generator for HERA Physics* (hamburg, Germany, 1999) A. Doyle, H. Jung and G. Grindhammer, Eds, p.329–346,DESY 99–067, MPI–PhE/99–02, hep–ph/9906441.

[12] A. RINGWALD AND F. SCHREMPP, In *New Trends in HERA Physics 1999* (Tegernsee, Germany, 1999), pp. 203, hep–ph/9909338.

[13] H1 COLLAB., S. AID ET AL., NUCL. PHYS. B480 (1996) 3.

[14] H1 COLLAB., S. AID ET AL., Z. PHYS. C72 (1996) 573.

[15] T. CARLI AND M. KUHLEN, NUCL. PHYS. B 511 (1998) 85 .

[16] PARTICLE DATA GROUP, C. CASO *et al.*, *Eur. Phys. J C 3* (1998) 1.

[17] A. RINGWALD AND F. SCHREMPP, In *Proc. DIS 2000* (Liverpool, England, 2000), J. Dainton, Ed., pp. DESY 00–089, hep–ph/0006215.

[18] H. JUNG, *Comp. Phys. Comm. 86* (1995) 147, see updates on http://www.desy.de/∼jung.

[19] M. Bengtsson and T. Sjöstrand, *Z. Phys. C 37* (1998) 465.

[20] V.N. Gribov and L.N. Lipatov, *Sov. J. Nucl. Phys. 15* (1972) 438; Yu.L. Dokshitzer, Sov. Phys. JETP 46 (1977) 641; G. Altarelli and G. Parisi, Nucl. Phys. 126 (1977) 297.

[21] B. Andersson et al., *Phys. Rep. 97* (1983) 81.

[22] T. Sjöstrand, *Comp. Phys. Comm. 39* (1986) 347; T. Sjöstrand and M. Bengtsson,ibid. 43 (1987) 367.

[23] L. Lönnblad, *Comp. Phys. Commun. 71* (1992) 15.

[24] G. Gustafson and U. Petterson, *Nucl. Phys. B 306* (1988) 741; G. Gustafson, Phys. Lett. B 175 (1986) 453; B. Andersson, G. Gustafson, L. Lönnblad and U. Petterson, Z. Phys. C 43 (1989) 625.

[25] L. Lönnblad, *Z. Phys. C 65* (1995) 285.

[26] A. Kwiatkowski, H. Spiesberger and H.-J. Möhring, *Comp. Phys. Comm. 69* (1992) 155.

[27] R. Engel, *Z. Phys. C 66* (1995) 203.

[28] CTEQ Collab., H.L. Lai et al., *Phys. Rev. D 55* (1997) 1280.

[29] N. Brook et al., In *Monte Carlo Generator for HERA Physics* (Hamburg, Germany, 1999), A. Doyle, H. Jung, and G. Grindhammer, Eds., p. 10.

[30] M. Gibbs, A. Ringwald and F. Schrempp, In *Proc. DIS 1995* (Paris, France, 1995), J.-F. Laporte and Y. Sirois, Eds., pp. 341–344, hep–ph/9506392.

[31] A. Ringwald and F. Schrempp, *to be published in Comp. Phys. Commun.* (1999) hep–ph/9911516.

[32] G. Marchesini et al., *Comp. Phys. Commun. 67* (1992) 465.

[33] B. Webber, *Nucl. Phys. **B** 238* (1984) 492.

[34] H1 Collab., I. Abt et al., *Nucl. Instr. and Meth. A 386* (1997) 310.

[35] H1 Collab., B. Andrieu et al., *Nucl. Instr. and Meth. A 336* (1993) 460.

[36] H1 Collab., B. Andrieu et al., *Nucl. Instr. and Meth. A 344* (1994) 492.

[37] H1 Collab., B. Andrieu et al., *Nucl. Instr. and Meth. A 372* (1996) 399.

[38] H1 Spacal Group, R.D. Appuhn et al., *Nucl. Instr. and Meth. A 386* (1997) 397.

[39] J. Bürger et al., *Nucl. Instr. and Meth. A 279* (1989) 217.

[40] H1 Collab., C. Adloff et al., *Eur. Phys. J. C 13* (2000) 609.

[41] L. Pozo, *University of Cambridge, RALT-002* (1993).

[42] CDF COLLAB., F. ABE ET AL., Phys. Rev. D 45 (1992) 1458.

[43] J. GERIGK, *Dipl. Thesis University of Hamburg (unpublished) and MPI-PhE/98-20* (Nov. 1998).

[44] H1 COLLAB., C. ADLOFF ET AL., *XXIX Int. Conf. on HEP, paper: 520, Vancouver (Canada)* (1998).

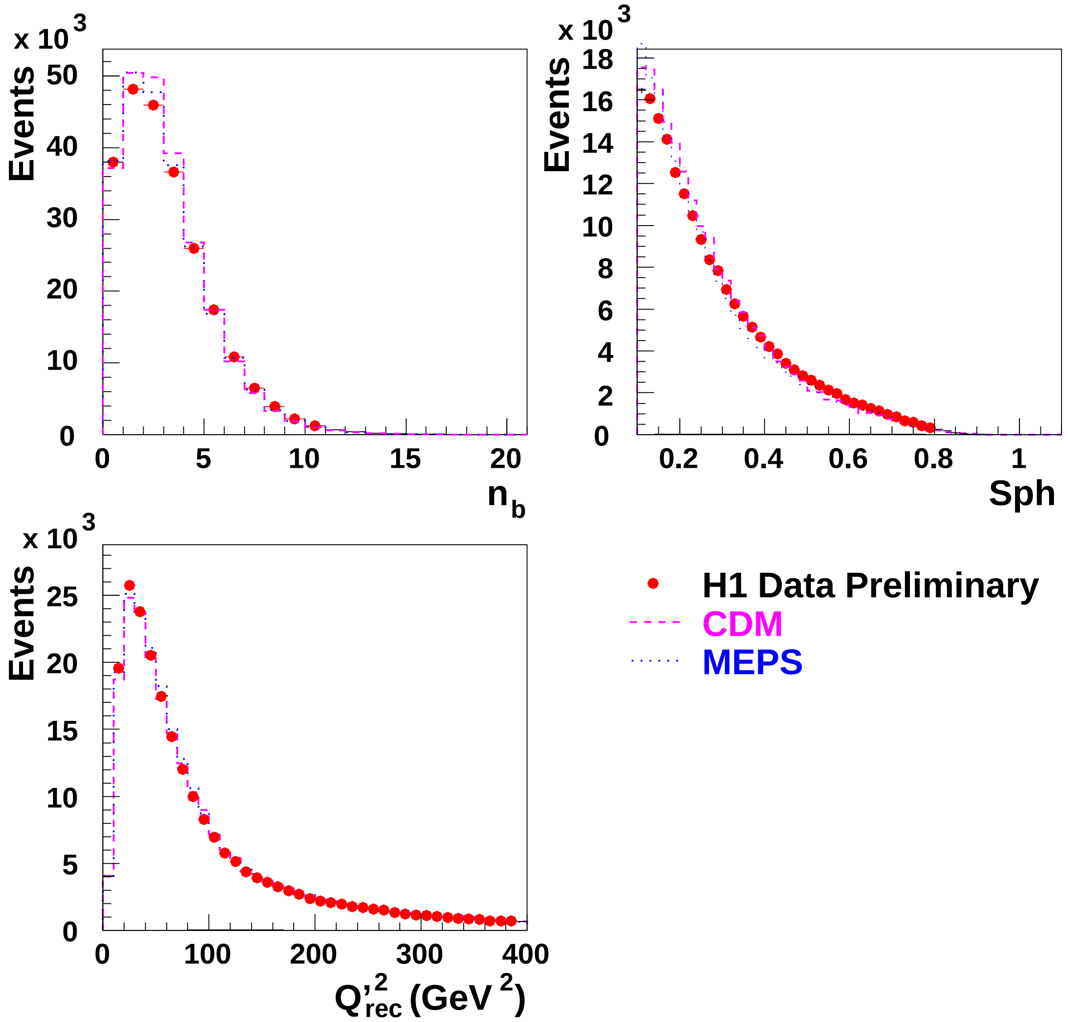

Figure 2: Distribution of the number of charged particles in the instanton band, of the sphericity in the rest system of all the final state objects not associated to the current jet and of the reconstructed Q'^2_{rec}. Shown are data and simulations of standard DIS events before cuts to enhance the instanton signal. The predictions for the instanton induced process are too small to be visible. The luminosity of the Monte Carlo simulation was scaled to the luminosity of the data.

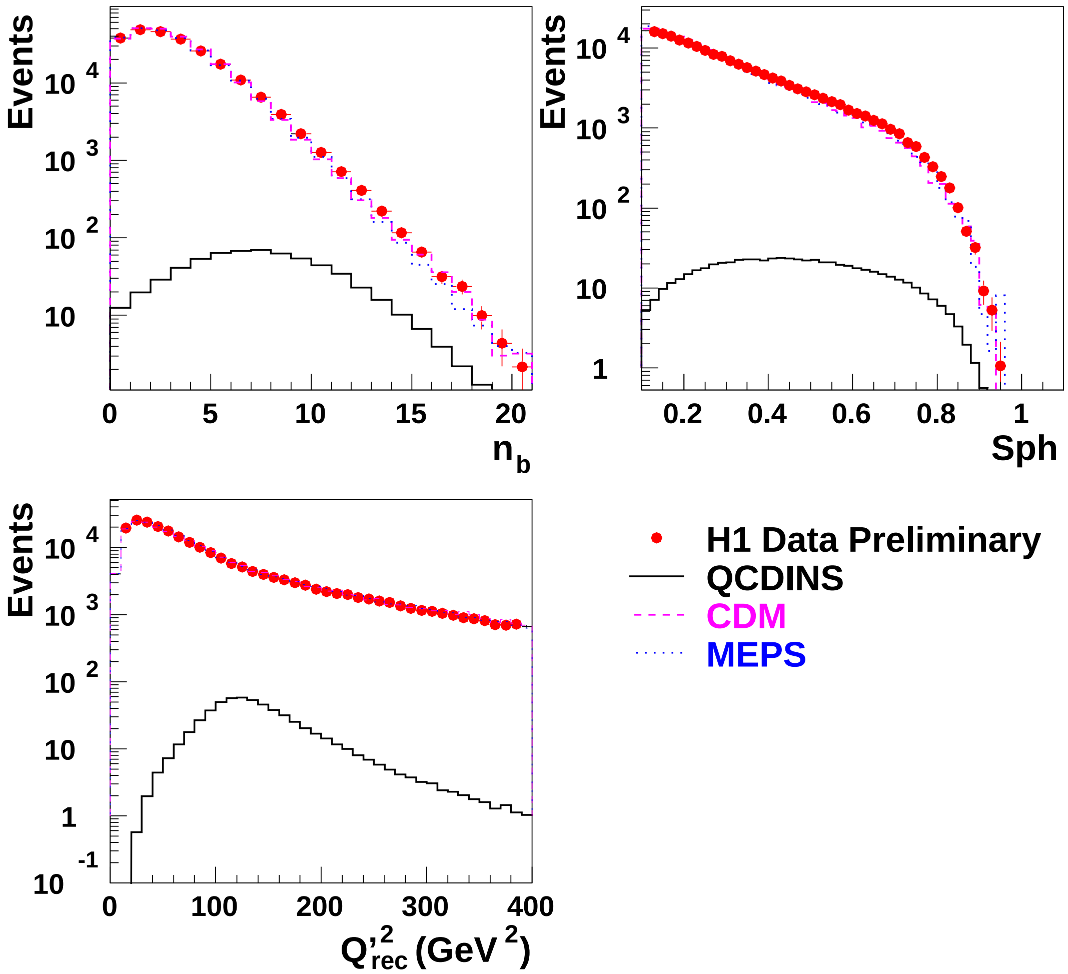

Figure 3: As Fig. 2, but with logarithmic scale. As explained in the text, the instanton events have been generated for $Q'^2 > 113\ \mathrm{GeV}^2$, as required theoretically. The apparent penetration of I-events into the region of smaller Q'^2 is due to the limited accuracy of the Q'^2 reconstruction and the experimental resolution.

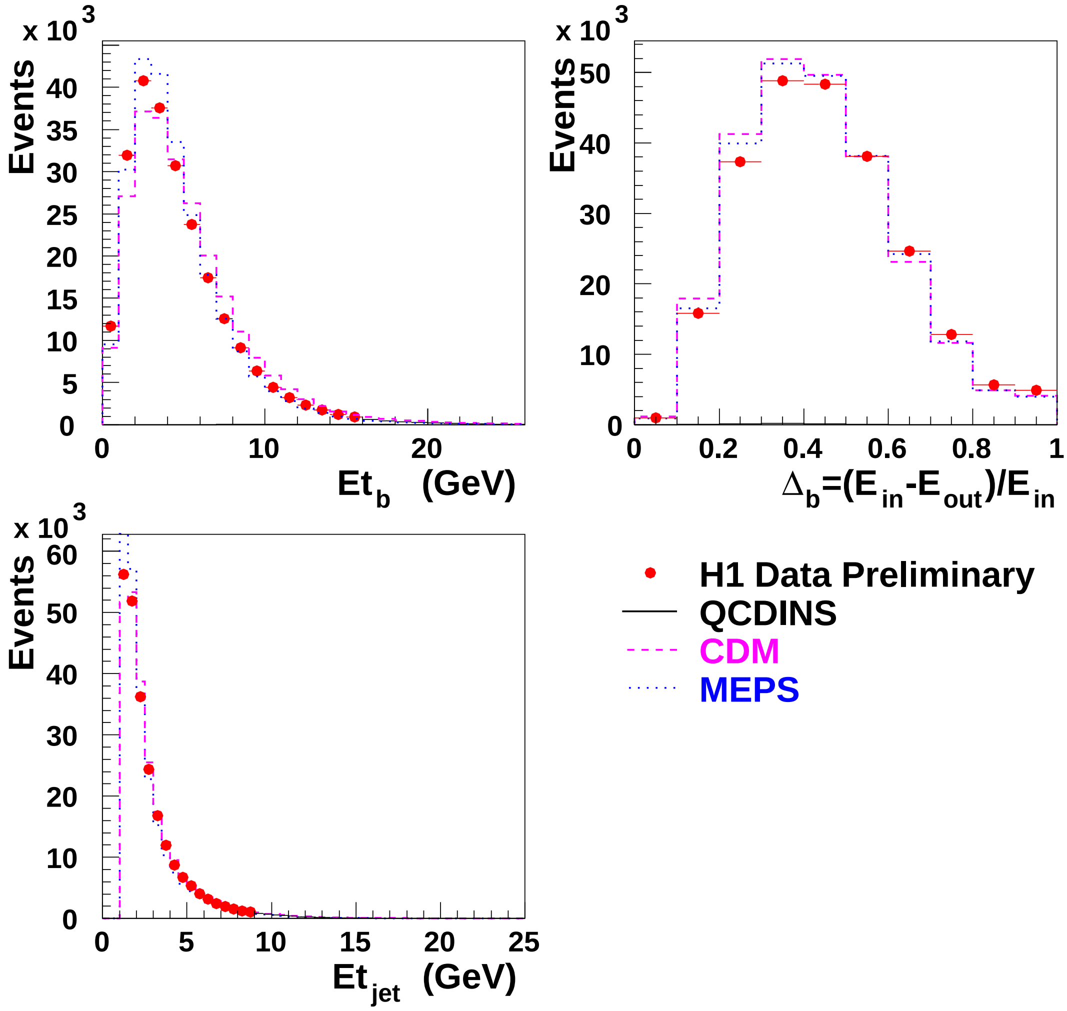

Figure 4: Distribution of the total E_t in the band, of $(E_{in} - E_{out})/E_{in}$ and of the transverse jet energy in the inclusive DIS sample. The luminosity of the Monte Carlo was scaled to the luminosity of the data.

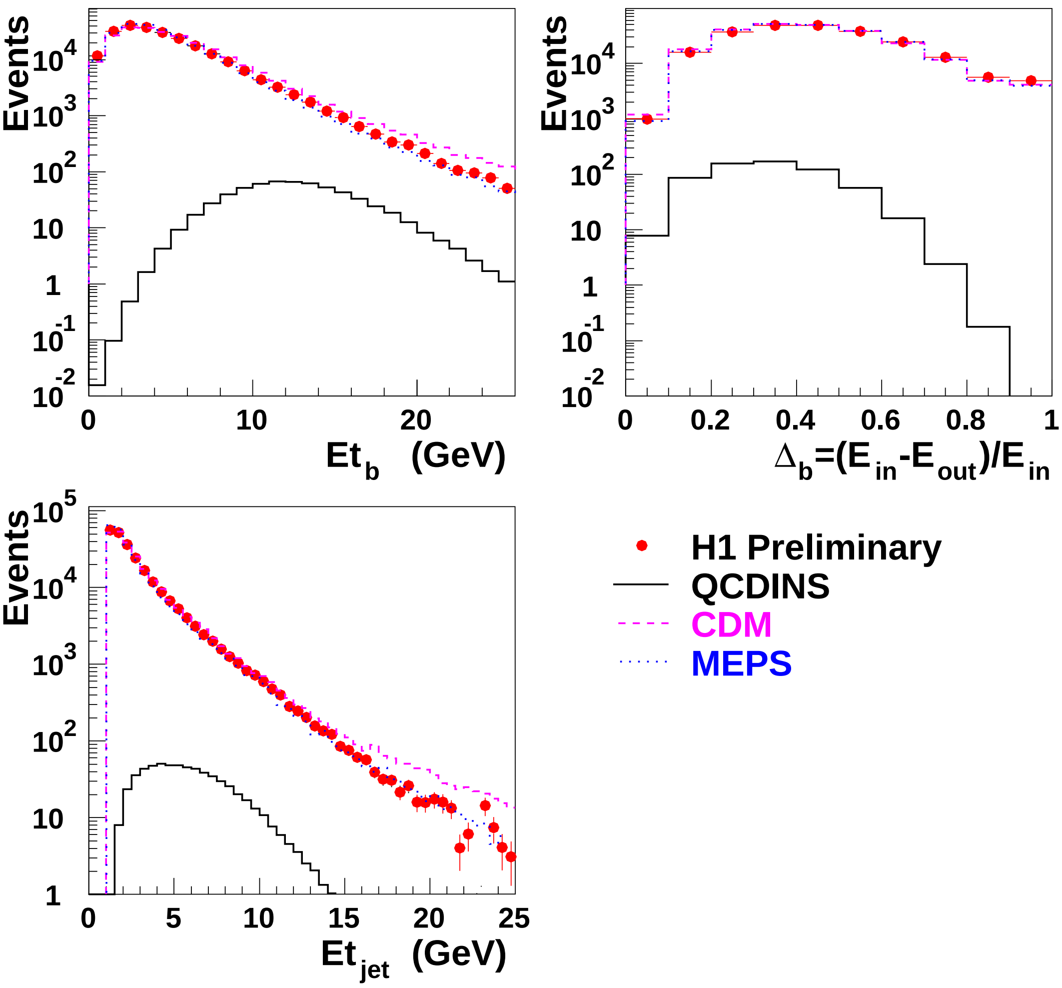

Figure 5: Same as Fig. 4, but in logarithmic scale.

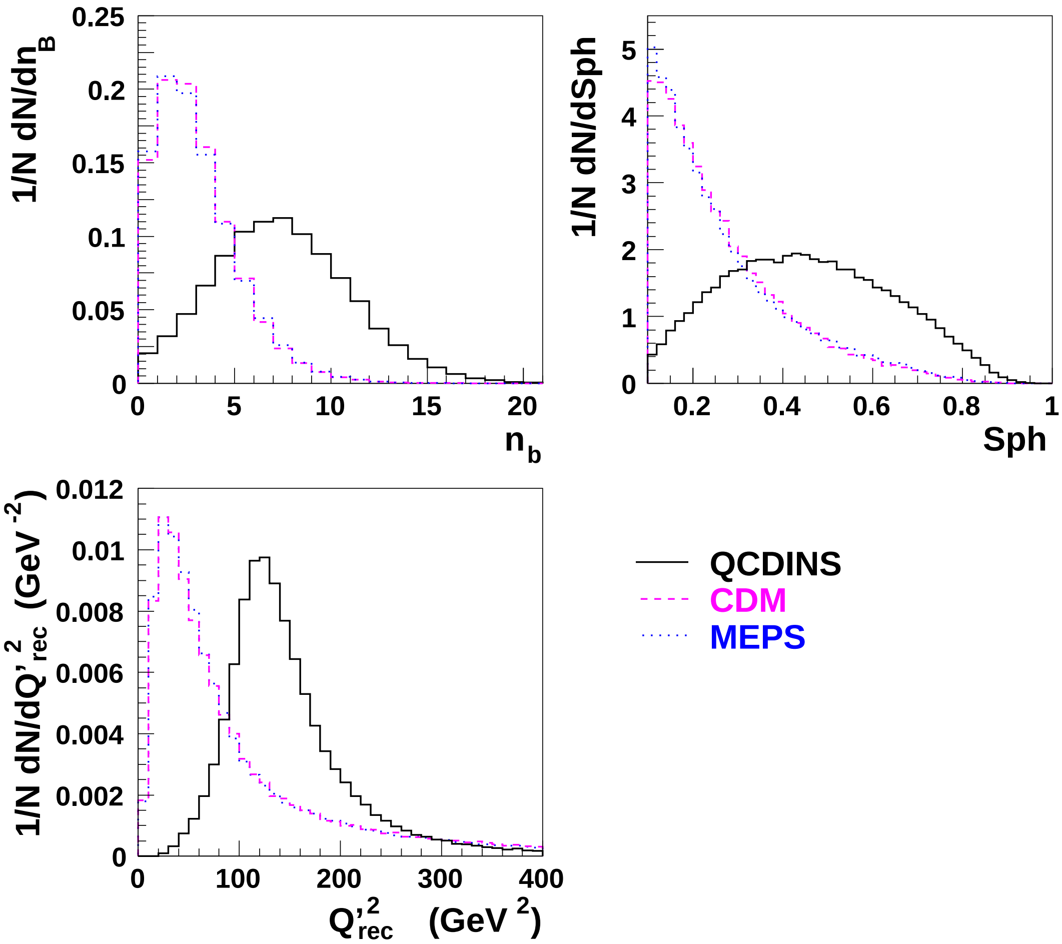

Figure 6: Shape normalised distribution of the number of charged particles in the instanton band, of the sphericity in the rest system of all the final state objects not associated to the current jet and of the reconstructed Q'^2_{rec}. Shown are standard DIS events and the instanton signal.

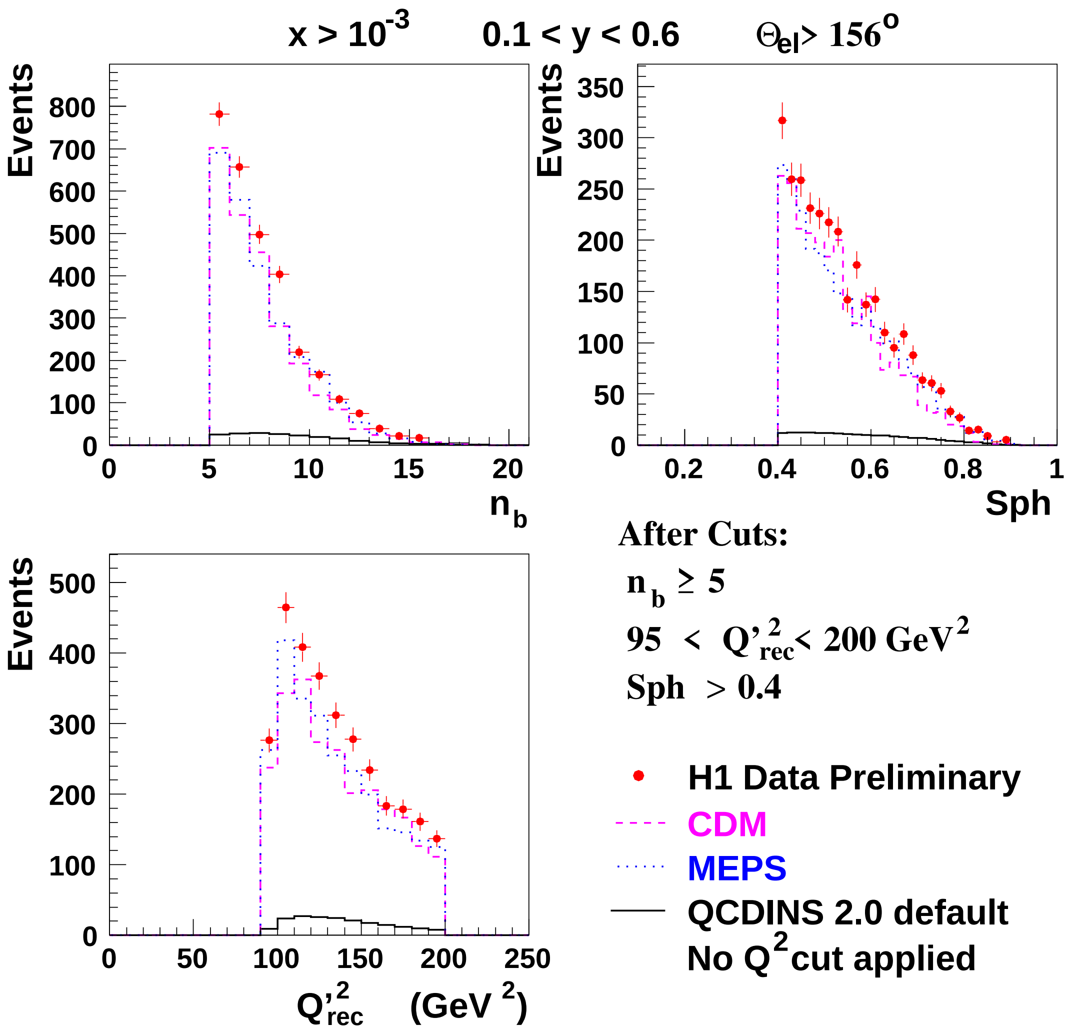

Figure 7: Distribution of the number of charged particles in the instanton band, of the sphericity in the rest system of all the final state particles not associated to the current jet and of the reconstructed Q'^2_{rec}. Shown are data and the predictions for instanton induced processes and standard DIS events after cuts to enhance the instanton signal. The luminosity of the Monte Carlo simulation was scaled to the luminosity of the data. The indicated cuts are called scenario A in the text.

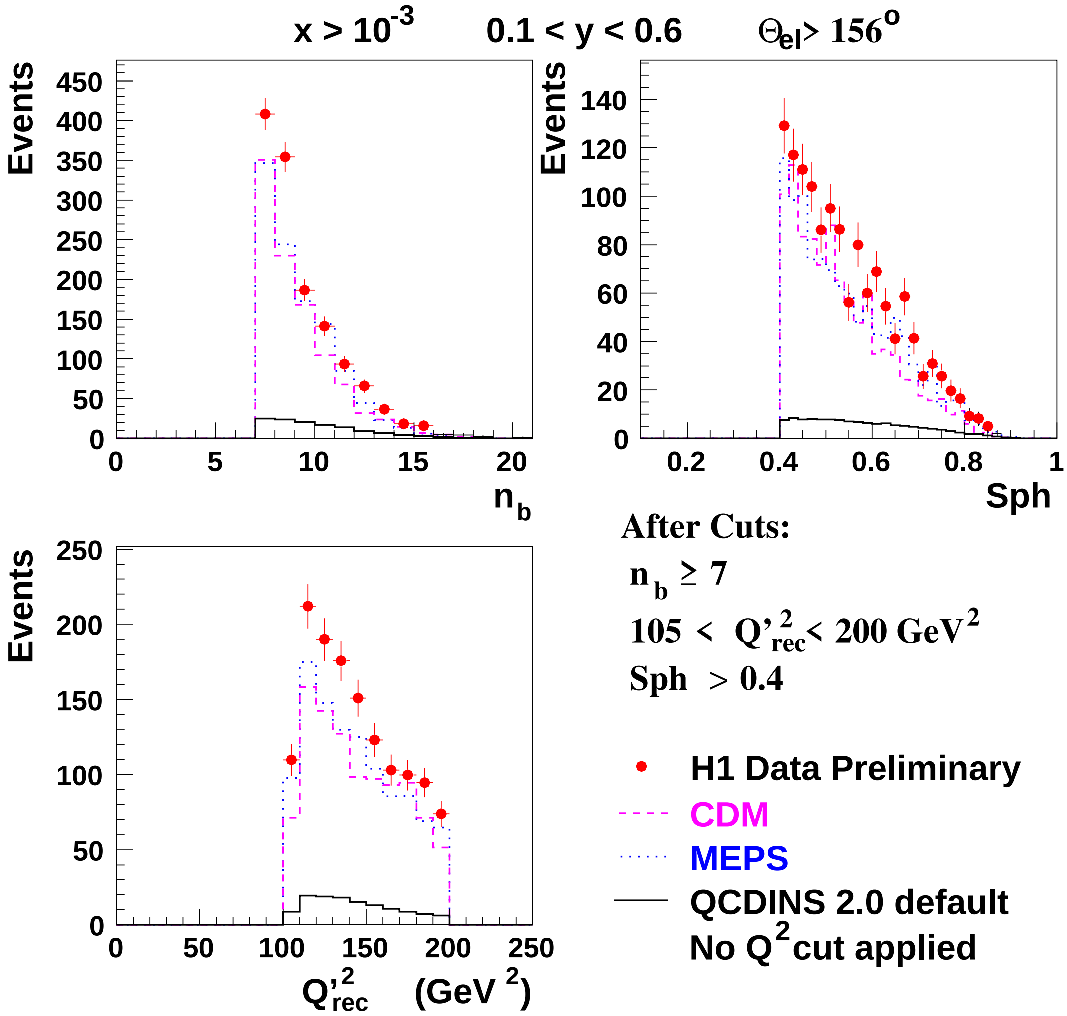

Figure 8: Distribution of the number of charged particles in the instanton band, of the sphericity in the rest system of all the final state particles not associated to the current jet and of the reconstructed Q'^2. Shown are data and the predictions for instanton induced processes and standard DIS events after cuts to enhance the instanton signal. The luminosity of the Monte Carlo simulation was scaled to the luminosity of the data. The indicated cuts are called scenario B in the text.

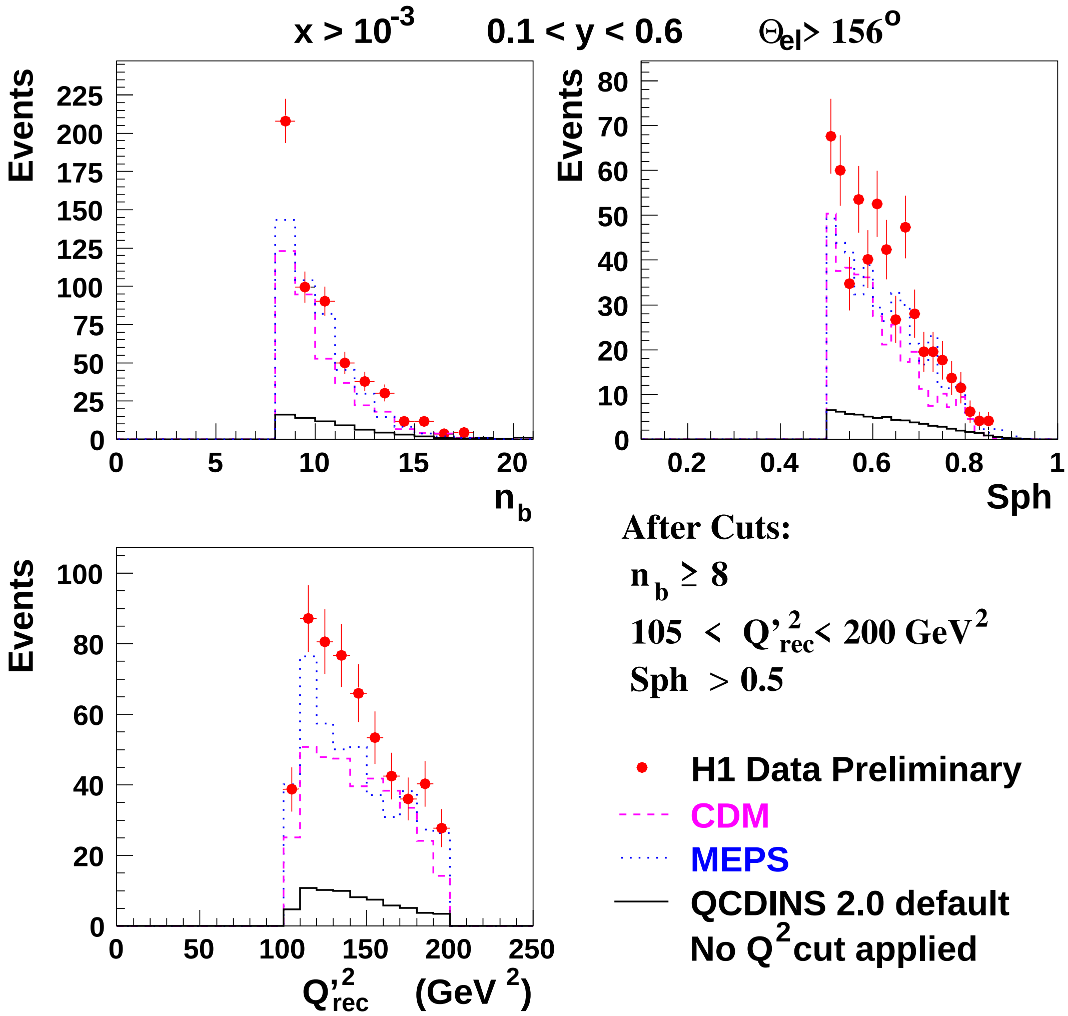

Figure 9: Distribution of the number of charged particles in the band, of the sphericity in the rest system of all the final state particles not associated to the current jet and of the reconstructed Q'^2 . Shown are data and the predictions for instanton induced processes and standard DIS events after cuts to enhance the instanton signal. The luminosity of the Monte Carlo simulation was scaled to the luminosity of the data. The indicated cuts are called scenario C in the text.

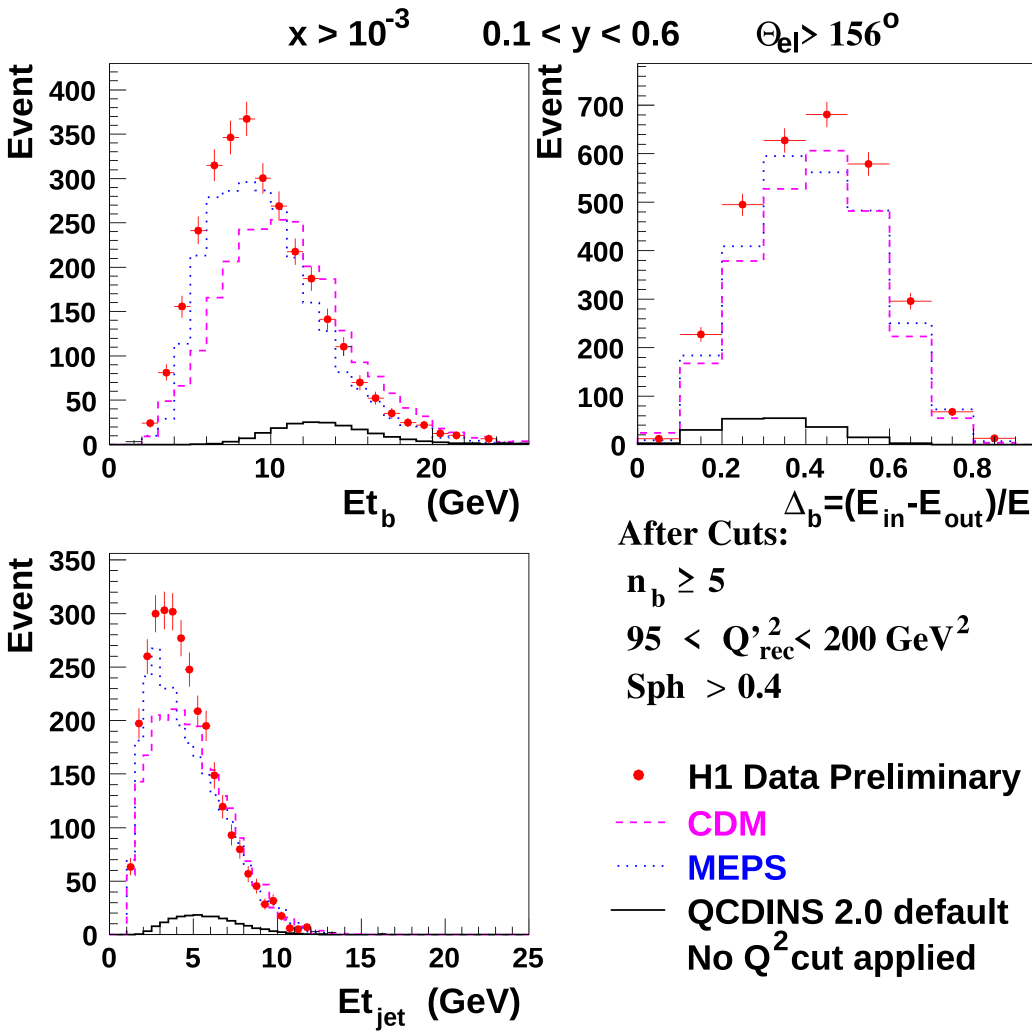

Figure 10: Distribution of the total E_t in the instanton band', of $(E_{in} - E_{out})/E_{in}$ and of the transverse jet energy after cuts to enhance the instanton signal. The luminosity of the Monte Carlo simulation was scaled to the luminosity of the data. The indicated cuts are called scenario A in the text.

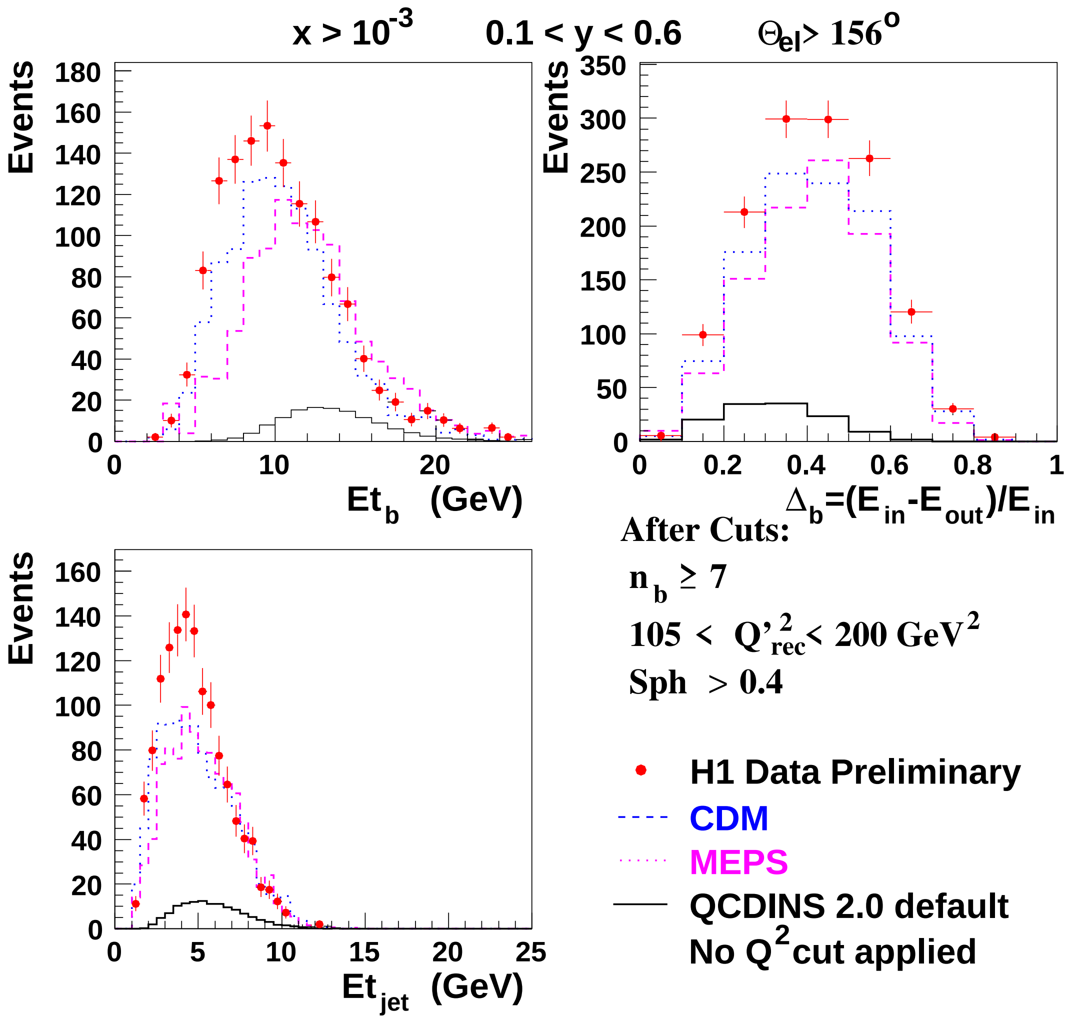

Figure 11: Distribution of the total E_t in the band, of $(E_{in} - E_{out})/E_{in}$ and of the transverse jet energy after cuts to enhance the instanton signal. The luminosity of the Monte Carlo simulation was scaled to the luminosity of the data. The indicated cuts are called scenario B in the text.

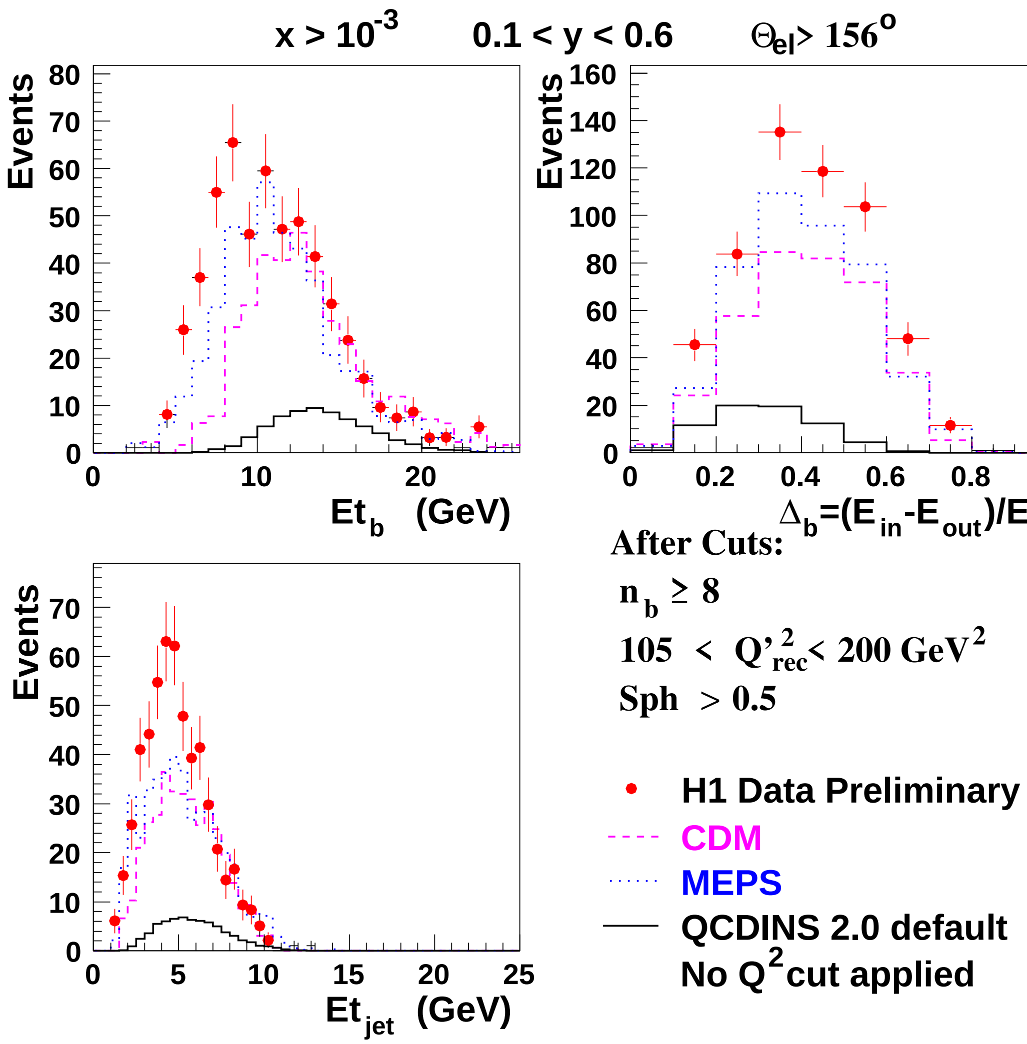

Figure 12: Distribution of the total E_t in the band, of $(E_{in} - E_{out})/E_{in}$ and of the transverse jet energy in the band after cuts to enhance the instanton signal. The luminosity of the Monte Carlo was scaled to the luminosity of the data. The indicated cuts are called scenario C in the text.

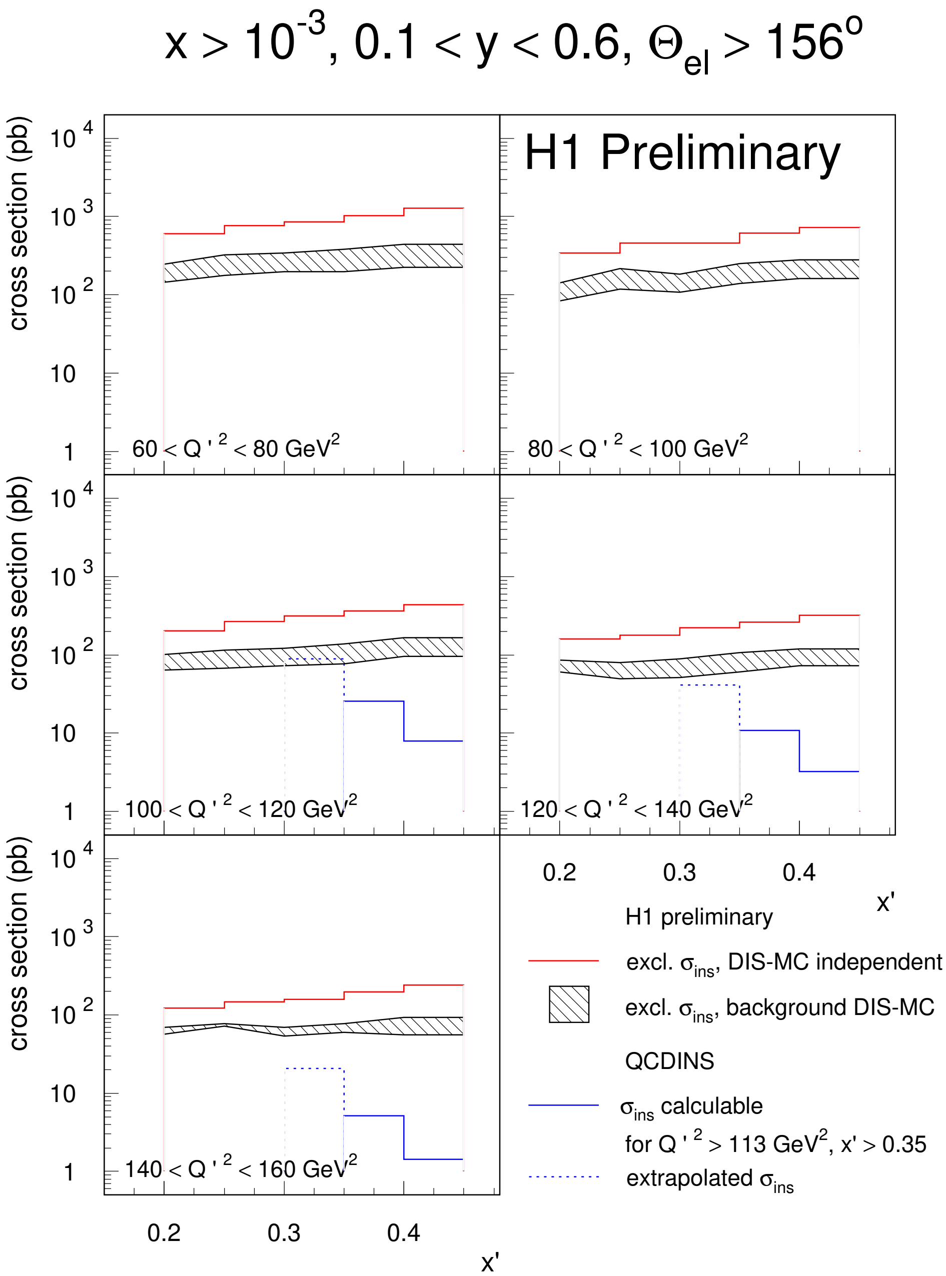

Figure 13: Upper limit on the cross section for instanton induced events as modelled by the QCDINS simulation as a function of x' in bins of Q'^2 . Regions above the curves are excluded. Also shown is the instanton cross section predicted in the fiducial region $x' > 0.35$ and $Q'^2 > 113\ \mathrm{GeV}^2$.